



Small-Scale Variability in the Nocturnal Boundary Layer

L. Mahrt¹  · Lena Pfister² · Christoph K. Thomas²

Received: 15 April 2019 / Accepted: 12 August 2019 / Published online: 17 September 2019
© The Author(s) 2019

Abstract

Nocturnal variations of temperature and wind are examined at three contrasting sites. After the early evening period of rapid cooling, the magnitude of the variations of temperature on a time scale of 10 min to an hour often become larger than the corresponding temperature change due to the nocturnal trend. These shorter-term temperature variations are forced by wave-like motions and more complex modes. Observations from a network of stations across a shallow valley at one of the sites are analyzed in more detail. Typically, decreasing wind speed corresponds to less mixing and lower temperature at the surface followed by increasing wind speed, increased mixing, and higher temperatures. The flow may continue to switch back and forth between these two states for much of the night. These non-stationary motions interact with motions induced by the gentle local topography, leading to intermittent local drainage flows, transient cold pools, and both propagating and semi-stationary microfronts.

Keywords Microfronts · Nocturnal boundary layer · Non-stationarity · Stratified turbulence · Submeso

1 Introduction

The stable boundary layer is often partitioned into a weakly stable regime of significant turbulence intensity and a very stable regime with lower turbulence intensity, which is often intermittent. However, Monahan et al. (2015) finds that traditional stability parameters alone are inadequate for partitioning the stable boundary layer. The causes of the variability of the turbulence in the more stable regime are not precisely known, although some of the variability is attributed to non-turbulent submeso motions (Acevedo et al. 2014) that include microfronts and wind direction shifts (Lang et al. 2018), internal gravity waves (Sun et al. 2015b), nearly horizontal two-dimensional modes (Mortarini et al. 2016), locally generated large-scale structures (Ansorge and Mellado 2014), and more complex modes. These motions collectively perturb the local flow (e.g., Monti et al. 2002; Sun et al. 2015a; Vercauteren et al. 2016; Cava et al. 2019a).

✉ L. Mahrt
mahrt@nwra.com

¹ NorthWest Research Associates, 2171 NW Kari Pl, Corvallis, OR 97330, USA

² Micrometeorology Group, University of Bayreuth, 95540 Bayreuth, Germany

Intermittent bursts of turbulence and associated warming are common and occur on a variety of time scales in the stable boundary layer (e.g., Nappo 1991; Ohya et al. 2008; Tampieri et al. 2015; Burman et al. 2018), although their relation to the non-turbulent motions is not always clear. The very stable boundary layer also includes short periods of particularly low turbulence intensity and lower temperatures that may last minutes (Zeeman et al. 2015) or tens of minutes (Mahrt 2017c). These micro cold events are sometimes well defined with sharp edges and arrive as microfronts (Zeeman et al. 2015; Kang et al. 2015; Lang et al. 2018; Grudzielanek and Cermak 2018). Cold air can originate over colder surfaces related to even weak heterogeneity of the soil and vegetation (Van de Wiel et al. 2002) or may be generated in cloud-free areas embedded within a general cloud cover and then advect over adjacent surfaces.

Vercauteren et al. (2016, 2019) find that stable conditions can be partitioned into subclasses based on whether or not submeso motions are significant and generate significant turbulence. Stable conditions can also be subdivided based on whether or not the submeso horizontal motions are separated in scale from the largest turbulence eddies (partial spectral gap). Without a clear separation of scales, the turbulence may not be able to maintain equilibrium with the changing submeso flow. Petenko et al. (2019) finds a general absence of organized temperature variations in thin very stable boundary layers except for sporadic elevated bursts of turbulence. However, in the deeper, less stable boundary layer, they find two subclasses, one with significant organized submeso variation of temperature and one without such structure. Acevedo et al. (2014), Vercauteren et al. (2019), and others have emphasized that the nature of the submeso motions varies between sites. The unpredictable variation of temperature and wind speed and direction on small time scales and the site differences are of considerable practical interest with respect to dispersion, frost occurrence and fog forecasting (Izett et al. 2018).

Momen and Bou-Zeid (2017) explicitly identifies the role of the time scale of the forcing through numerical examination of the response of the turbulence to a non-stationary horizontal pressure gradient. When the time scale of the forcing by the perturbation pressure gradient is large compared to the characteristic time scale of the turbulence (a scale gap), the turbulence maintains approximate equilibrium with the forcing. In contrast, the turbulence does not maintain equilibrium when the forcing time scale is the same order of magnitude as the turbulence time scale (no scale gap).

Mortarini et al. (2017) details the potential complexity of nocturnal boundary layers due partly to the interaction between the turbulence and a variety of submeso motions as well as circulations driven by surface heterogeneity and associated low-level jets. Cava et al. (2019b) examines formation of a low-level jet that follows the collapse of the turbulence. Subsequently, the low-level jet generates mixing below the wind maximum. Intermittent turbulence and associated warm and cold events in the stable nocturnal boundary layer can be induced by even modest microtopography (Pfister et al. 2017; Mahrt 2017c). Guerra et al. (2018) found that the microtopography induces horizontal variation of temperature that systematically increases with decreasing wind speed. Based on fine-scale measurements of the horizontal structure, Pfister et al. (2019) found that spatial and temporal variations of temperature on horizontal scales of a few 100 m or less in gentle topography tended to organize into several prototype regimes: windy with limited formation of cold air; windy but with cold air drainage and pooling modulated by large shear-induced mixing and lee turbulence; and low wind speeds with more robust cold-air drainage and cold pool formation. This organization was formulated in terms of the general wind speed, stratification, and downward longwave radiation. These forcing variables were found to be interdependent but not to the extent that one of them could be eliminated.

To examine these interactions, measurements from three sites are investigated. After describing the datasets, we contrast the statistics of the non-turbulent changes of temperature between the sites. We then focus on a case-study night that reveals the interaction between the impact of weak local topography and transient motions.

2 Observations and Analysis

The Shallow Cold Pool (SCP) Experiment was conducted over semi-arid grasslands in north-east Colorado, USA, from 1 October to 1 December 2012 (https://www.eol.ucar.edu/field_projects/scp). See Mahrt and Thomas (2016) for more information on this site. The main valley is relatively small, roughly 12 m deep and 270 m across (Fig. 7, Sect. 5.2). The width of the valley floor averages about 5 m with an average down-valley slope of 2%, increasing to about 3% at the upper end of the valley. The side slopes of the valley are on the order of 10% or less. We analyze the 1-m sonic anemometer observations from 20 stations and from the main tower at 0.5, 1, 2, 3, 4, 5, 10, and 20 m. The SCP measurements include fiber-optic distributed temperature sensing (DTS) (Thomas et al. 2012; Zeeman et al. 2015; Pfister et al. 2017, 2019), which provides fine horizontal resolution of 0.3 m and time resolution of 5 s at 0.5, 1, and 2 m above the ground surface along a 250-m cross-valley transect. Times are expressed in local standard time (LST = UTC – 7 h). For examination of the time structure of events, decimal time is used.

The second field campaign contains measurements from sonic anemometer measurements collected in North Park, Colorado, USA, in 2002, during the Fluxes Over a Snow Surface II field program (*FLOSSII*, <http://www.eol.ucar.edu/isf/projects/FLOSSII/>) within the North Park Basin (Mahrt and Thomas 2016). On average, the valley floor is about 30 km wide with valley sidewalls of 1000 m over a horizontal width of about 7 km. The basin is approximately 50 km from south to north. The surface consists of matted grass, sometimes with a shallow snow cover. The roughness length for this site is quite small, less than 1 mm with snow cover. Scattered short brush occurs beginning 100–200 m upwind with respect to the prevailing southerly flow.

The third set of observations were collected during the CASES-99 (Cooperative Atmospheric Surface Exchange Study) over grassland in south-central Kansas, USA (Poulos et al. 2001; Sun et al. 2002). This dataset is only of 1-month duration but includes a 60-m tower and has become a standard for analysis of the nocturnal boundary layer. We analyze sonic anemometer measurements taken at 1.5 m for the first part of the program and then moved to 0.5 m for the remainder of the field program.

2.1 Averaging

Our analysis approach is detailed in Mahrt and Thomas (2016). The flow is partitioned as

$$\phi = \phi' + \bar{\phi}, \quad (1)$$

where the overbar designates a time average over a window of width τ , chosen here to be 1 min. ϕ' is the deviation from such an average. ϕ is potential temperature or one of the velocity components. The heat flux is computed as $w'\theta'$, where w' is the perturbation vertical velocity. The wind speed is determined as

$$U \equiv \sqrt{\bar{u}^2 + \bar{v}^2}. \quad (2)$$

We also compute the standard deviation of the vertical velocity fluctuation within the averaging window, σ_w , as a measure of the turbulence intensity.

A local potential temperature at each station is defined with respect to the base of the tower on the valley floor by using the dry adiabatic lapse rate between the absolute elevation of the base of the tower (Z_{base}) and the absolute elevation of the 1-m level at a given station (Z) such that the potential temperature at a given station is

$$\theta \equiv T + 0.01(Z - Z_{\text{base}}), \quad (3)$$

with height in m. Station A1 is the highest station where the 1 m level is 20 m above the base of the tower. For time series, θ is expressed in °C.

3 Short-Term Variability Versus Nocturnal Trend

We begin with a simple statistical assessment of time variability of temperature in the nocturnal boundary layer. The temperature change, $\delta_t(\theta)$, is defined to be the difference of θ between two adjacent half window means with a total window width of τ_F . If the averages for each half window are considered to represent the midpoint of their respective half window, then $\delta_t\theta$ (K) estimates the variation of θ over $\tau_F/2$ because $\tau_F/2$ is the distance between the midpoints of two half windows. Nominally, $\tau_F/2$ is chosen to be 1 h. This window sequentially moves through the record 1 min at a time, corresponding to considerable overlap of the windows. We average $\delta_t\theta$ over all windows in a given field program to compute $[\delta_t\theta]$. For each window, we require that $\{w'\theta'\} < -0.003 \text{ Km s}^{-1}$ to eliminate unstable and near-neutral conditions where the heat flux may be too small to adequately estimate. Curly brackets refer to averaging over the window. We also require that $\{R_{\text{net}}\} < -20 \text{ W m}^{-2}$. This requirement removes overcast conditions and also removes most of the rapid cooling period during the evening transition when the positive net radiation decreases with time and reverses to negative net radiation (Mahrt 2017b). With this condition, there is no need to apply time of day restrictions.

As the window moves sequentially through the record, it samples structures with random phase and variable sign of $\delta_t\theta$. An estimate of the contribution of the nocturnal trend to $\delta_t\theta$ is constructed by averaging $\delta_t\theta$ (sign retained) over all of the windows such that $[\delta_t\theta]$ becomes an estimate of the average nocturnal temperature decrease over the time interval $\tau_F/2$. This averaging filters out small-scale time variability, which has no sign preference. Averaging the absolute values to compute $[\text{abs}(\delta_t\theta)]$ provides an estimate of the total temperature variation that includes both the systematic nocturnal variation and the smaller-scale variations that contain both positive and negative values.

A measure of the smaller-scale temperature variations can be expressed as

$$[\delta_t\theta]_{sm} \equiv [\text{abs}(\delta_t\theta)] - \text{abs}([\delta_t\theta]), \quad (4)$$

where again $[\text{abs}(\delta_t\theta)]$ is the average of the total variation and $[\delta_t\theta]$ is the temperature difference due to the nocturnal trend, hereafter referred to as simply the nocturnal trend. We refer to $[\delta_t\theta]_{sm}$ as the small-scale (submeso) temperature variability, which is the variability not explained by the nocturnal trend.

3.1 Differences Between the Small-Scale Variations and the Nocturnal Trend

We now examine the dependence of the total variation, $[\text{abs}(\delta_t\theta)]$, on the window width τ_F . For station A1 outside the valley at the SCP site, $[\text{abs}(\delta_t\theta)]$ increases with increasing $\tau_F/2$ (black, Fig. 1) due to the capture of a larger range of non-stationary motions. $[\text{abs}(\delta_t\theta)]$ is

Fig. 1 Dependence of cooling on $\tau_F/2$ at Station A1 outside the valley at the SCP site. $\tau_F/2$ is the width over which temperature changes are estimated. The magnitude of the total temperature variation, $[\text{abs}(\delta_t\theta)]$ (K, black), includes contributions from both the nocturnal trend and the smaller-scale variations. $[\delta_t\theta]$ (K, red) is an estimate of the average nocturnal trend

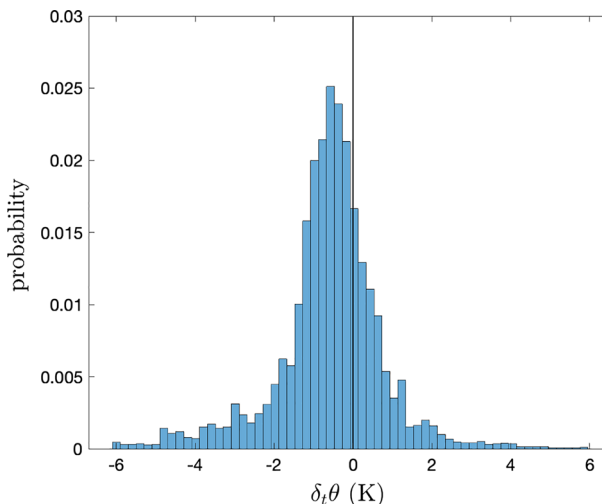
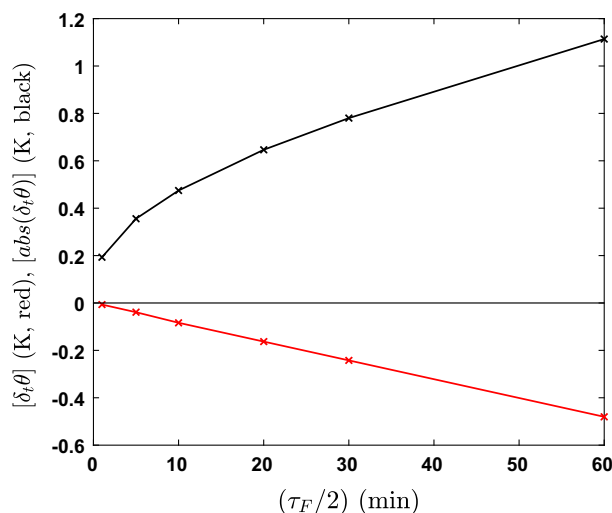


Fig. 2 The frequency distribution of $\delta_t\theta$ at SCP station A1 outside of the valley for $\tau_F/2 = 60$ min

a little more than 1 K for $\tau_F/2 = 1$ h. Because the temperature difference $[\delta_t\theta]$ increases approximately linearly with $\tau_F/2$, the cooling rate due to the nocturnal trend ($[\delta_t\theta]/(\tau_F/2)$) is approximately independent of $\tau_F/2$. The effect of the choice of the window width on the above statistics is similar to that at the FLOSSII and CASES-99 sites.

The frequency distribution of $\delta_t\theta$ for $\tau_F/2 = 60$ min at the SCP station A1 (Fig. 2) indicates that the total variation $\delta_t\theta$ is a combination of the submeso temperature variations and an approximate -0.5 K shift due to the nocturnal trend. The frequency distribution indicates that the magnitude of $\delta_t\theta$ for individual sampling windows is often large compared to the magnitude of the nocturnal trend. The average nocturnal trend over a 1-h period (Table 1) is about 0.5 K h at the FLOSSII and SCP sites and is 0.6 K at the CASES-99 site. Recall that these results include windy nights and partly cloudy conditions, which reduce the averaged nocturnal cooling compared to clear nights with low wind speeds. At the FLOSSII

Table 1 Site, the averaged temperature change due to the nocturnal trend, $[\delta_t \theta]$, the averaged absolute temperature change $[\text{abs}(\delta_t \theta)]$, and the estimate of the small-scale time variability of temperature, $[\delta_t \theta]_{sm}$

Site	$[\delta_t \theta]$	$[\text{abs}(\delta_t \theta)]$	$[\delta_t \theta]_{sm}$	$P (\%)$
<i>FLOSSII</i>	−0.50	1.12	0.61	34
<i>SCP A1</i>	−0.48	1.11	0.63	35
<i>SCP A9</i>	−0.48	1.12	0.63	35
<i>SCP A11</i>	−0.50	1.23	0.73	37
<i>CASES-99</i>	−0.60	1.06	0.46	27

Temperature differences are estimated over the time interval $\tau_F/2 = 60$ min. P is the percent of the values of $\delta_t \theta$ that are positive, counter to the sign of the nocturnal trend

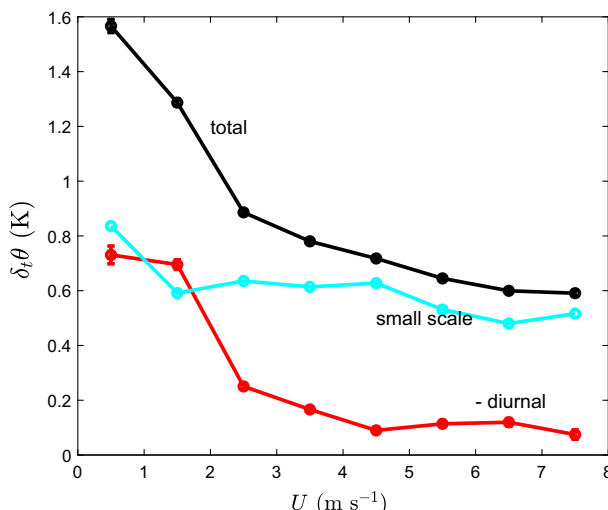


Fig. 3 The 1-m temperature difference $\delta_t \theta$ at the FLOSSII site for $\tau_F/2 = 60$ min. The dependence of the total temperature variation ($[\text{abs}(\delta_t \theta)]$, black), the negative of the nocturnal trend ($-\delta_t \theta$, red), and the inferred small-scale time variability of temperature ($[\delta_t \theta]_{sm}$, cyan) on the wind speed, U . Here, the operator $[\cdot]$ is an average over all of the samples for the entire field program for a given interval (bin) of the wind speed

and SCP sites, the submeso temperature variation, $[\delta_t \theta]_{sm}$, averages about 30% more than the magnitude of the nocturnal trend, depending on the station. $[\delta_t \theta]_{sm}$ is a little smaller than the magnitude of the nocturnal trend at the CASES-99 site probably because of flatter terrain.

We define P as the probability of $\delta_t \theta > 0$; that is, the probability that the 1-h temperature change is opposite to the expected nocturnal trend. With no small-scale variability and only nocturnal trend, P is small because the nocturnal trend is generally negative. The probability P may approach 50% when the magnitude of the nocturnal trend is negligible compared to the small-scale variability because the small-scale temperature variability shows no sign preference. The probability P is about 35% for both the FLOSSII and SCP sites (Table 1), implying that the magnitude of the small-scale temperature variability is important; P is only 27% for the CASES-99 site where the intensity of the submeso motions is lower.

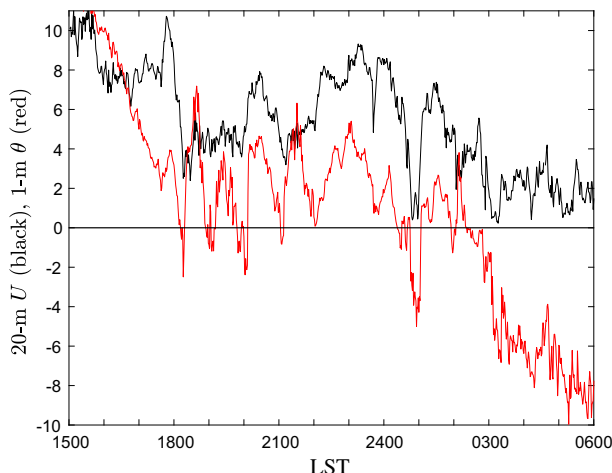


Fig. 4 Observations at the tower for night 24–25 November in the SCP field program. Shown are the 20-m wind speed U (m s^{-1} , black) and θ at 1 m on the tower ($^{\circ}\text{C}$, red) relative to the night-averaged temperature

3.2 Dependence on Wind Speed

The magnitude of the nocturnal temperature trend is normally expected to be larger with low wind speeds and clear skies. However, the dependence of the temperature variation on the wind speed, net radiative cooling, and stratification is complicated at the SCP site because the net radiative cooling, on average, increases with increasing wind speed. The very lowest wind speeds, less than 1 m s^{-1} , are often associated with cloudy conditions. Clear skies and significant radiative cooling induce drainage/down-valley flows and thus prevent very low wind speeds. In addition, the relationship between the wind and stratification at the SCP site depends partly on the wind direction through horizontal temperature advection (Mahrt 2017a).

The temperature changes at the FLOSSII site depend more systematically on the wind speed U . As expected, the magnitude of the nocturnal trend (Fig. 3a, red) decreases systematically with increasing U . The small-scale time variability of temperature, $[\delta_t \theta]_{sm}$ (cyan), is more independent of U so that the small-scale temperature variability becomes relatively more important for larger U . One might have thought that the greater mixing with large U would reduce $[\delta_t \theta]_{sm}$. However, horizontal temperature variations more effectively generate local time variations with larger advecting velocity.

The overall statistics for the FLOSSII site (Table 1) are significantly influenced by the frequent low wind speeds $< 2 \text{ m s}^{-1}$ at the FLOSSII site where the magnitude of the nocturnal trend increases to values comparable to those for $[\delta_t \theta]_{sm}$ (Fig. 3). The plotted error bars in Fig. 3 are generally too small to be seen, although the standard error neglects the large dependence between samples and might seriously underestimate the uncertainty. $[\delta_t \theta]_{sm}$ also appears to depend significantly on the stratification and wind direction, currently under investigation.

4 Night of 24–25 November (DOY 329)

The above statistics indicate that the magnitude of the small-scale non-turbulent variations of temperature are often large compared to the magnitude of the nocturnal trend and motivate

the examination of individual cases that contribute to such variability. We concentrate on the SCP observations where the spatial coverage is extensive. We proceed with a case study based on the night of 24–25 November in the SCP field program, which includes multiple flow regimes (Fig. 4) and is one of the nights with fiber-optic DTS measurements. We partition the night into two main periods. The first period begins at 1800 LST, after the early evening period of rapid cooling, and extends to 0200 LST when the wind speed at the 20-m top of the tower decreases substantially to an averaged value of about 2 m s^{-1} (Fig. 4, black).

The second period from 0300 to 0600 LST is characterized by relatively low wind speeds even at 20 m (Fig. 4, black). The nocturnal cooling trend becomes large during this period due to the decreased wind speed and turbulence intensity. The flow is characterized by somewhat chaotic small-scale variations of temperature, which are lower amplitude compared to the first half of the night. There is no well-defined scale separation between the turbulent scales and the smallest non-turbulent motions.

We now examine the first half of the night when the nocturnal temperature trend is small, but the variations of temperature on a time scale of roughly 1 h are large, sometimes exceeding 5 K (red, Fig. 4). We concentrate on stations A1 located west of the valley system, A3 in an up-valley tributary gully, A11 on the valley floor, A9 on the slope north of the valley, and the 20-m level of the main tower. See Fig. 8 (Sect. 5) for station locations. The flow is characterized by periods of higher wind speed and generally higher temperatures and periods of lower wind speed and generally lower temperatures (Fig. 5). These time variations of the wind speed and temperature are not closely approximated by a wave pattern because the amplitude varies with time, and sometimes the variations with time are relatively sharp, particularly near the surface. Such small-scale variations of wind and temperature affect the entire network with only small phase differences across the network, and thus are on a horizontal scale that is larger than the 500-m wide observational domain. These variations also extend above the 20-m tower.

The well-defined minimum values of temperature are separated by about 1 h (Fig. 5a). $\theta(A11)$ on the valley floor often becomes much lower than the temperature outside the valley (A1) or on the slope (A9) such that the temperature minimum on the valley floor is part of a transient cold pool (Fig. 5a). The temperature difference between the valley and outside the valley is as large as 7°C during periods of cold pools and can vanish between the periods of cold pools.

5 Case Study of Cooling and the Transient Cold Pool

We choose the period from 1900 to 2100 LST for further study of the development of a transient cold pool with a temperature minimum occurring at about 2000 LST (Fig. 6b). This study period includes the flow evolution leading up to the temperature minimum and subsequent rapid warming. From 19.2 to about 19.8 h, depending on the station, the cooling trend is roughly independent of time (Fig. 6b) and the wind direction is generally northwesterly (Fig. 6c), approximately aligned with the regional slope on a scale of 10–20 km. Just before 20 h, the wind direction generally shifts to south-westerly on the valley floor (for example, stations A8, A10, A11, and A16, Fig. 7) and west-south-westerly on the slope south of the valley (stations A12–A14). The stations on the valley floor experience an enhanced cooling rate during this brief period. This enhanced cooling is abruptly eliminated by a well-defined warm microfront that propagates through the entire network (Sect. 5.3).

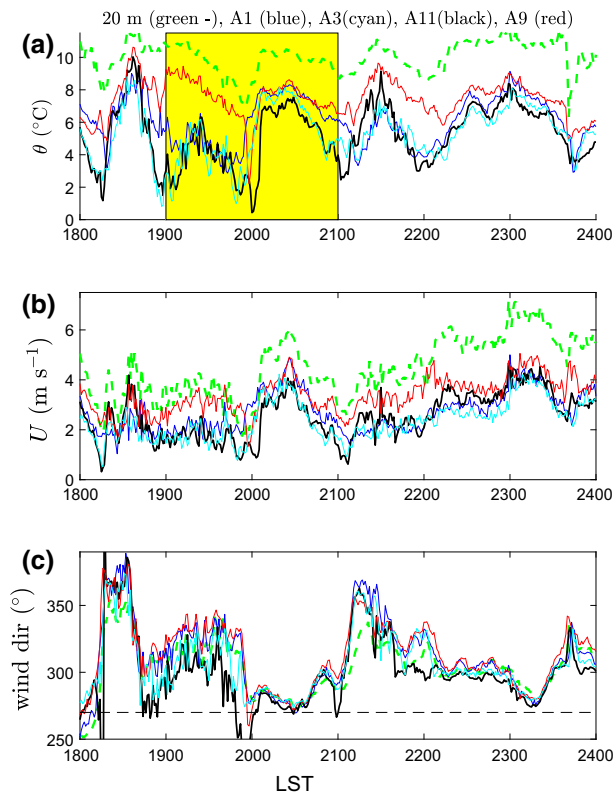


Fig. 5 The period of “higher” wind speed corresponding to the first half of the night. Shown are a) θ , b) U , and c) wind direction for five different stations (see Fig. 7 for station locations). The yellow shading identifies the period of focus for Sect. 5. Note that 360° has been added to north-easterly wind directions to avoid discontinuities. θ is the local potential temperature (Eq. 3)

5.1 The Local South-Westerly Flow

Downslope south-westerly flow develops on the slope south of the valley that ascends toward the south-west for a distance of about 750 m with an average slope magnitude of about 2.5%. At about 19.9 h, this south-westerly flow develops more or less simultaneously along the slope within the network (black, red, Fig. 6c) in association with the reduced north-westerly flow above the valley (green dashed, Fig. 6a, b).

The formation of the brief south-westerly flow occurs intermittently throughout the case study night. In the later half of the case study night when the wind speed is lower, the wind direction on the valley floor (not shown) sometimes oscillates between west-south-westerly and west-north-westerly flow. This oscillation includes station A12 just above the valley floor on the south-west slope. South-westerly flow south of the valley also occurs on other nights. The composite of the nocturnal wind vectors over the entire field program (not shown) indicates that the v-component is negative (northerly) at all of the stations except those on the slope south of the valley where it is approximately zero due to a significant number of cases of south-westerly flow. We conclude that cold-air drainage on the south-westerly slope is of climatic significance at this site. Cold-air drainage down the shorter slope north of the

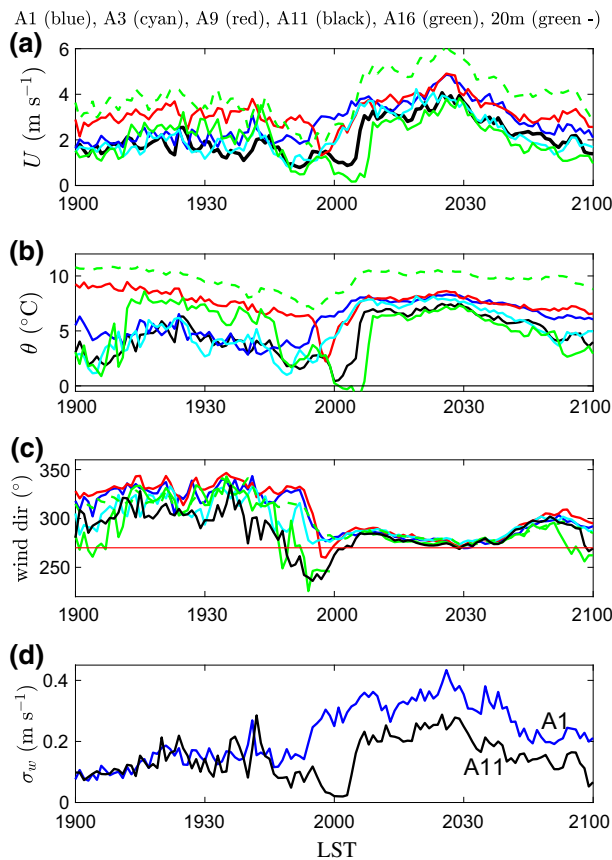


Fig. 6 The 2-h period surrounding the temperature minimum at 2000 LST for a) U , b) θ , c) wind direction, and d) σ_w . Dashed green is the 20-m level on the tower. The progression of the cold air down the shallow valley can be tracked from stations A3 (cyan), A11 (black), and A16 (green). $[\sigma_w]$ is shown for outside the valley at station A1 (blue) and on the valley floor at station A11 (black). See Fig. 7 for station locations

valley is uncommon, where lee turbulence is frequent with a northerly component of the larger-scale flow.

5.2 Transient Cold Pool and Upslope Advection

The temperature minimum on the valley floor can be viewed as a part of the transient cold pools. Brief enhanced local cooling occurs on the valley floor during the period of southwesterly flow (Fig. 6c). A minimum temperature of about 1.5°C occurs around 1951 LST at the up-valley gulley station A3 (Fig. 6b, cyan), about 0.4°C at about 2000 LST at the valley station A11 (black), and 1.0°C at about 2006 LST further down the valley at station A16 (green). Apparently the valley imposes sufficient sheltering with the decreasing wind speed (Fig. 6a) to allow formation of a transient cold pool. The transient cold pool is characterized by particularly low turbulence intensity as shown for station A11 on the valley floor (black line, Fig. 6d). In other terms, the minimum wind speed occurs as part of the 1-h variation of the wind field and leads to reduced turbulence and an enhanced cooling rate on the valley

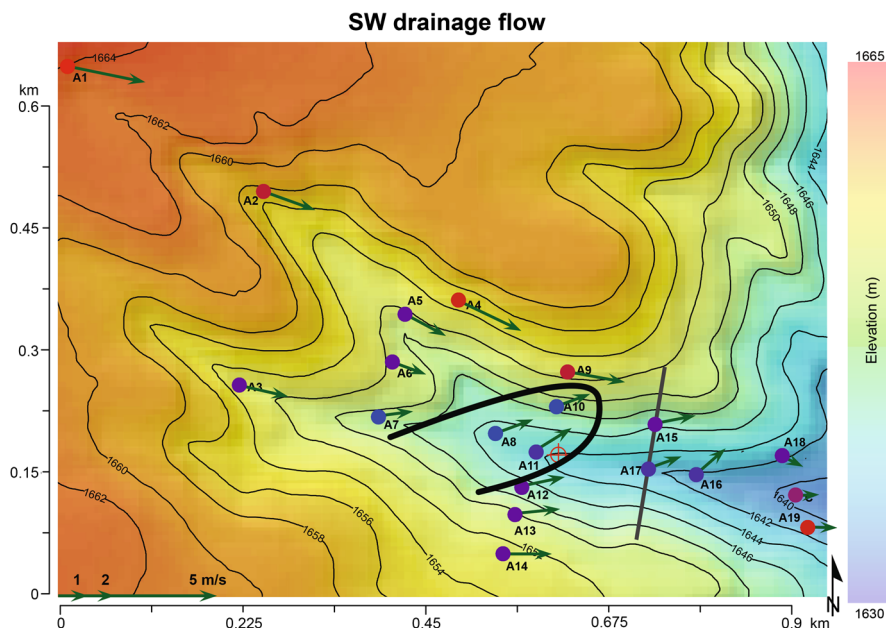


Fig. 7 The spatial distribution of the temperature and wind averaged over the 5-min period ending at 2000 LST. The temperature ranges from 1 °C (blue circles) to 6 °C (red circles). The solid black line roughly outlines the core of the south-west drainage flow. The thin grey line through stations A15 and A17 is the fiber-optic DTS transect. The red + marks the tower location

floor. This particular transient cold pool consists of a double structure at some of the stations divided by a very brief period of warmer air as is also evident in Figs. 9–10.

During the field program, cold events are also observed outside of the valley (not shown). The small-scale temperature variability at station A1 outside the valley is, on average, only about 15% less than that on the valley floor at station A11 (Table 1). However, the physics is different because the short-term temperature variation on the valley floor is typically associated with intermittent cold pools related to topographical sheltering.

An updraft observed in advance of the warm microfront causes adiabatic cooling that might contribute significantly to the total cooling. The vertical velocity on the tower reaches 0.1 m s^{-1} at the 3-m level and 0.2 m s^{-1} at the 20-m level. This updraft arrives too late to account for the initial rapid cooling but contributes to the formation of the coldest air occurring just after 20 h on the valley floor (A11).

The south-westerly flow advects cold air from the valley cold pool up the opposite slope north of the valley, causing cooling that reaches station A9 around 1957 LST (Fig. 6b, red). This corresponds to a displaced cold pool. This cold air then descends back down the slope and down the valley. In fact, the coldest air in the entire network occurs at station A10 on the slope north of the valley, located about 4 m above the elevation of the valley floor (not shown). The advection of the cold air up the slope north of the valley is also evident in the cross-valley fiber-optic DTS cross-section (Figs. 9, 10) where at 2000 LST the cold air (blue) briefly extends up-slope to the top of the fiber-optic DTS transect. For a brief period before 2000 LST, the air is colder on the slope than at the floor of the valley (Fig. 10). This displacement of the coldest air up the slope is common during the SCP field program. The northern edge of the cold air (dark blue) transitions to warm air (red) at a microfront that

Transient cold pool and advancing warm microfront

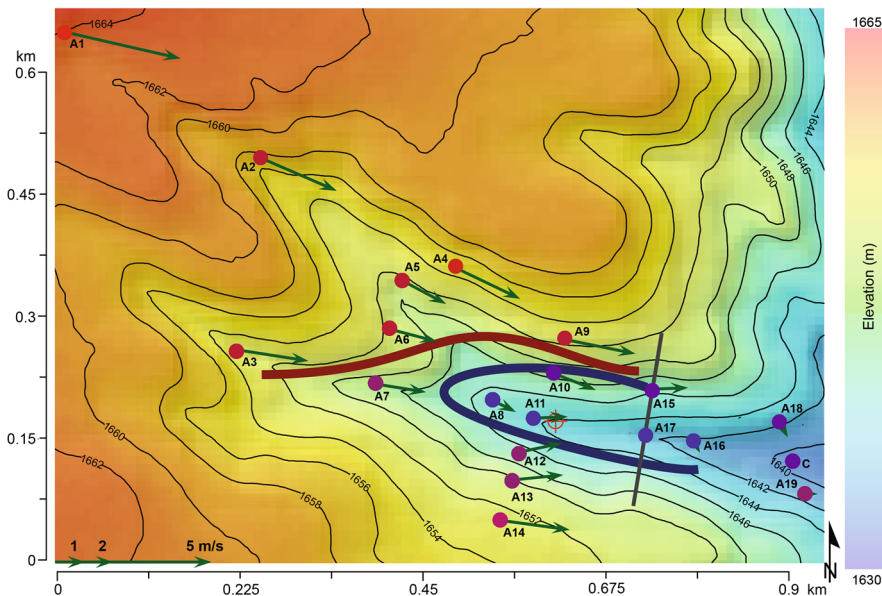


Fig. 8 The spatial distribution of the temperature and wind for the 5-min period beginning at 2000 LST. The temperature ranges from 1 °C (blue circles) to 6 °C (red circles). A plausible sketch of the warm microfront (thick red line), which propagates from the north-north-west in contrast to the surface wind, which is more from the west-north-west. Based on the tower observations, warm air passes over the transient cold pool (thick blue line) and then mixes downward to the valley floor. The thin grey line through stations A15 and A17 is the fiber-optic DTS transect. The red + marks the tower location

does not systematically propagate. This quasi-stationary microfront on the slope north of the valley appears intermittently throughout this night and appears on numerous other nights during the field program.

“Less cold” air on the slope south of the valley is evident in the fiber-optic DTS image that ends in a sharp semi-stationary microfront during the period 1948–2006 LST (light blue to dark blue transition in Figs. 9, 10). This microfront is temporary, does not systematically propagate, and is not particularly common on this slope during the field program.

5.3 Warm Microfront

The warm microfront quickly terminates the cooling trend and eliminates the transient cold pool in the valley, corresponding to a sudden increase of temperature, wind speed, and σ_w (Fig. 6). The enhanced mixing nearly eliminates horizontal variability in agreement with Guerra et al. (2018) and reduces both the stratification and wind directional shear (Fig. 11). The warm microfront begins at station A1 at about 1951 LST (blue, Fig. 6b) and propagates toward the south-east and then occupies the entire western part of the network by 2000 LST (see also Fig. 8). At this time, the warm air reaches A9 and A14 on the slopes north and south of the valley, respectively, but has not yet penetrated to the valley floor. The warm microfront invades the northern end of the fiber-optic DTS transect at about 2000 LST (Fig. 10) and then propagates toward the valley floor during a period of about 5 min. The warm air arrives at the south end of the fiber-optic DTS transect shortly before it reaches the valley floor, again

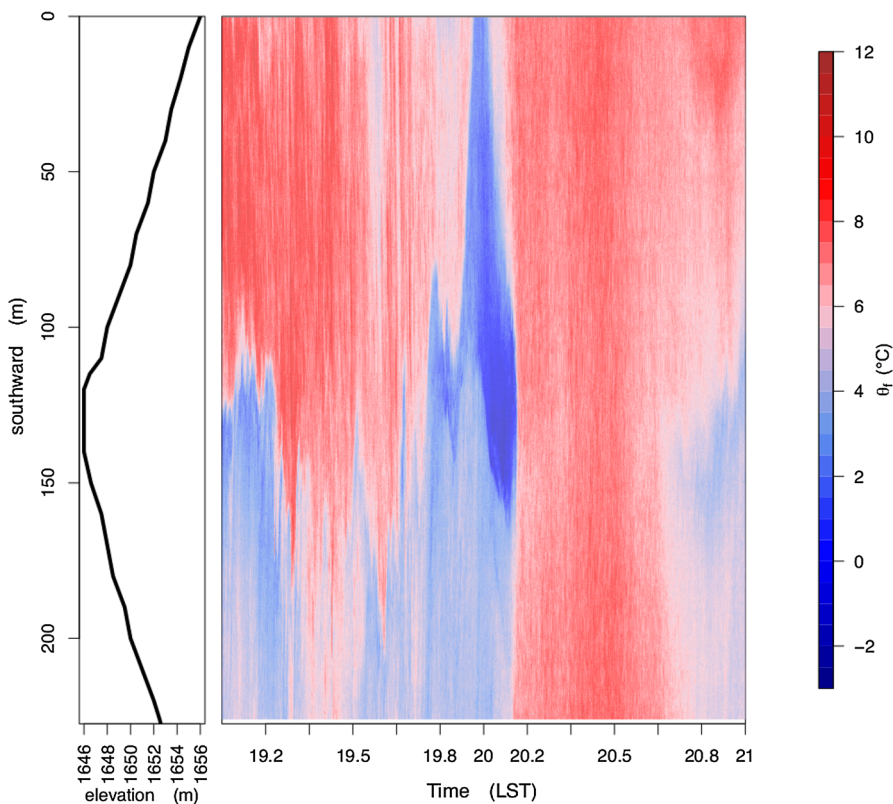


Fig. 9 The time–space variation of the local potential temperature measured by the fiber-optic DTS (θ_f). The coldest air arrives at the DTS cross-section at about 20.0 h (2000 LST). It is important to avoid interpreting the x -axis as space instead of time. The topography following the DTS transect is shown on the left. North is toward the top

indicating that for a few minutes the warm air moves over the cold air on the valley floor (Figs. 9, 10). At 2004 LST, the valley cold pool is quickly eliminated, probably by the warm air that is mixed downward by the “relatively” high turbulence intensity in the warm air.

The propagation direction of the warm microfront from the north-west is distinctly different from the wind direction, which is generally more westerly behind the warm microfront. The difference between the wind direction and the apparent direction of the warm microfront propagation could be at least partly related to warming at the surface by the relatively “strong” downward mixing of warmer air behind the warm microfront, in which case the temperature changes are not completely controlled by horizontal advection. Large misalignment between the microfront propagation and the wind direction is common in the observational study of Lang et al. (2018).

5.4 Vertical Structure

The vertical structure of the temperature measured on the 20-m tower (Fig. 11a) indicates that the amplitude of the cooling and the subsequent warming both decrease with height, but are still significant at the top of the tower. The warming within the shallow valley cold

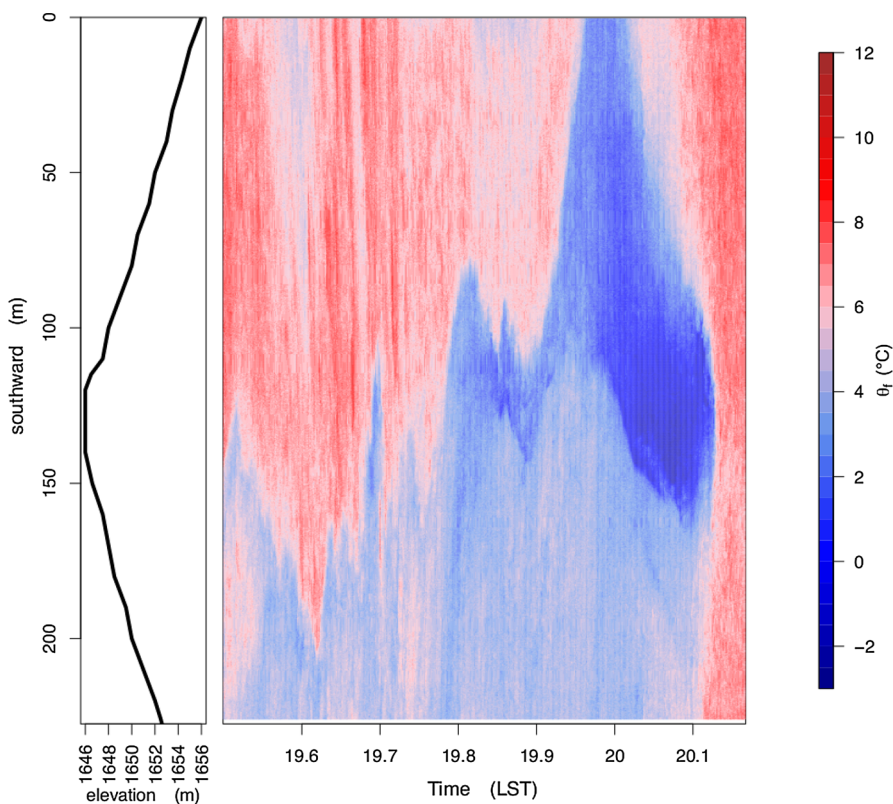


Fig. 10 A zoomed plot of the time-space variation of the local potential temperature measured by the fiber-optic DTS (θ_f) that focuses on the cold event (dark blue)

pool lags that at higher levels and lags the warming outside the valley. The near elimination of the wind directional shear after the warm microfront (Fig. 11b) is presumably due to the significant mixing following the warm microfront.

5.5 Synopsis

The cold event examined here is summarized in Fig. 12 and includes a period of relatively constant cooling rate (19.4–19.8 h, 1924–1948 LST), subject to short-term temperature fluctuations, and includes a period of more rapid cooling and development of drainage flows (19.8–20 h, 1948–2000 LST). A shallow transient cold pool forms on the valley floor followed by advection of cold air up the slope north of the valley floor. This cold event is quickly terminated by a sharp warm microfront (20.1 h, 2006 LST) that leads to significant vertical mixing, significant reduction of the stratification, and near elimination of horizontal variations of temperature within the observational domain.

Transient cold pools and temperature minimums are a common feature during the entire SCP field program and generally form during periods of reduced wind speed on time scales of 10 min to several hours. Wind speeds at 1 m that exceed about 2 m s^{-1} on the valley floor seem to eliminate the transient cold pools and maintain warmer air at the surface, although

Fig. 11 **a** The wind direction, and **b** temperature as a function of height on the tower for measurements at 0.5 m (blue), 1 m (red), 2 m (orange), 3 m (purple), 4 m (grey), 5 m (cyan), 10 m (dark red), and 20 m (blue)

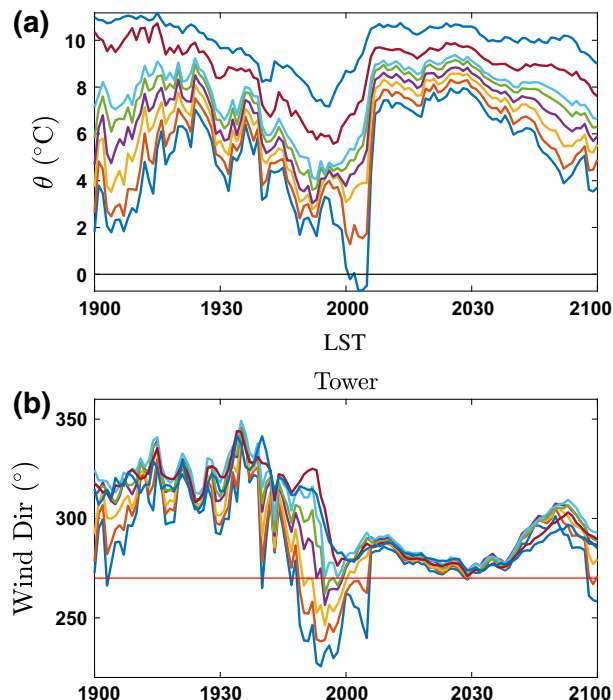
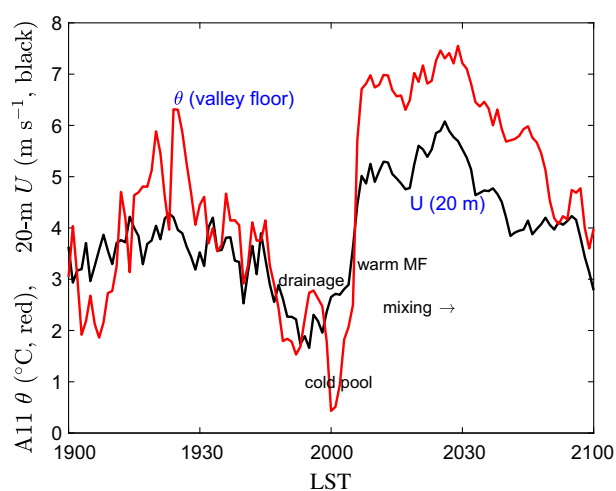


Fig. 12 A summary of the 2-h case study cold event based on the temperature at station A11 on the valley floor (red) and the wind speed at 20 m (black)



this “threshold” appears to vary between stations. This threshold wind speed is higher than the threshold wind speed for the “hockey stick” (Sun et al. 2012), which is about 1.2 m s^{-1} based on the dependence of the 1-m friction velocity on wind speed for the current SCP measurements outside of the valley (Pfister et al. 2019). The higher threshold for the cold pool compared to that for the usual hockey stick is probably due to the influence of sheltering by the topography and associated strong stratification. As a result, the cold-pool threshold also depends on the wind direction.

6 Conclusions

After the early evening period of rapid cooling, small-scale (submeso) temperature variations often become larger than the magnitude of the nocturnal temperature trend (Sect 3). As a consequence of the small-scale temperature variations, the nocturnal temperature actually increases over 1-h periods about 35% of the time at the FLOSSII and SCP sites and 27% of the time at the CASES-99 site. The generality of these results and the complexities of the physics behind these statistics are currently under investigation.

The large variations of temperature on small time scales at the SCP site appear to be due to transient propagating modes that interact with the local modest topography. Spatial and time variation of the temperature, wind, and other quantities associated with the propagating modes can be locally intensified near the surface, sometimes forming cold or warm microfronts. For the first part of the case study night, semi-periodic variations of the wind speed on a time scale of about 1 h range between 1 and 4 m s^{-1} and modulate the turbulence and temperature. Higher-speed periods correspond to greater turbulence intensity and higher temperatures while periods of lower wind speed correspond to lower turbulence intensity and lower temperatures, as expected. During the phases of lower wind speed, local slope circulations and cold pools develop, which are eliminated during the periods of higher wind speeds. Thus, local flows intermittently form and disappear. The second part of the night is characterized by low wind speeds, generally less than 2 m s^{-1} , and includes a large cooling trend with smaller and less organized small-scale variability of temperature.

The small-scale propagating motions and the motions induced by the gentle local topography interact in a way that remains poorly understood. We anticipate that these interactions are globally common. On nights with significant small-scale variations of temperature, even perfect forecasts of the nocturnal trend may fail to identify important short periods of frost or fog formation. The relation of such temperature variations to the wind vector, stratification, downward longwave radiation, and the general magnitude of the small-scale motions must be investigated in more detail, both in terms of cases studies and classification of nights (Pfister et al. 2019).

Acknowledgements We gratefully acknowledge the very helpful comments of the anonymous reviewers. This project received support from Grant AGS-1614345 from the National Science Foundation. The fiber-optic instrument was provided by the Center for Transformative Environmental Monitoring Programs (CTEMPs) funded by the National Science Foundation through award EAR 0930061. The measurements for the SCP and FLOSSII field programs were provided by the Integrated Surface Flux System of the Earth Observing Laboratory of the National Center for Atmospheric Research. The assistance of C. Sayde in the collection and processing the fiber optic DTS data is greatly appreciated.

Open Access This article is distributed under the terms of the Creative Commons Attribution 4.0 International License (<http://creativecommons.org/licenses/by/4.0/>), which permits unrestricted use, distribution, and reproduction in any medium, provided you give appropriate credit to the original author(s) and the source, provide a link to the Creative Commons license, and indicate if changes were made.

References

- Acevedo O, Costa F, Oliveira P, Puhales F, Degrazia G, Roberti D (2014) The influence of submeso processes on stable boundary layer similarity relationships. *J Atmos Sci* 71:207–225
- Ansorge C, Mellado J (2014) Global intermittency and collapsing turbulence in a stratified planetary boundary layer. *Boundary-Layer Meteorol* 153:89–116
- Burman PKD, Prabha TV, Morrison R, Karipot A (2018) A case study of turbulence in the nocturnal boundary layer during the Indian summer monsoon. *Boundary-Layer Meteorol* 169:115–138

Cava D, Mortarini L, Anfossi D, Giostra U (2019a) Interaction of submeso motions in the Antarctic stable boundary layer. *Boundary-Layer Meteorol* 171:151–173

Cava D, Mortarini L, Giostra U, Acevedo O, Katul G (2019b) Submeso motions and intermittent turbulence across a nocturnal low-level jet: a self-organized criticality analogy. *Boundary-Layer Meteorol* 172:17–43

Grudzielanek AM, Cermak J (2018) Temporal patterns and vertical temperature gradients in micro-scale drainage flow observed using thermal imaging. *Atmosphere* 9:498–514

Guerra VS, Acevedo OC, Medeiros LE, Oliveira PES, Santos DM (2018) Small-scale horizontal variability of mean and turbulent quantities in the nocturnal boundary layer. *Boundary-Layer Meteorol* 169:395–411

Izett JG, van de Wiel BJH, Baas P, Bosveld FC (2018) Understanding and reducing false alarms in observational fog prediction. *Boundary-Layer Meteorol* 169:347–372

Kang Y, Belušić D, Smith-Miles K (2015) Classes of structures in the stable atmospheric boundary layer. *Q J R Meteorol Soc* 141:2057–2069

Lang F, Belušić D, Siems S (2018) Observations of wind direction variability in the nocturnal boundary layer. *Boundary-Layer Meteorol* 166:51–68

Mahrt L (2017a) Heat flux in the strong-wind nocturnal boundary layer. *Boundary-Layer Meteorol* 163:161–177

Mahrt L (2017b) The near-surface evening transition. *Q J R Meteorol Soc* 143:2940–2948

Mahrt L (2017c) Stably stratified flow in a shallow valley. *Boundary-Layer Meteorol* 162:1–20

Mahrt L, Thomas CK (2016) Surface stress with non-stationary weak winds and stable stratification. *Boundary-Layer Meteorol* 159:3–21

Momen M, Bou-Zeid E (2017) Mean and turbulence dynamics in unsteady Ekman boundary layers. *J Fluid Mech* 816:209–242

Monahan A, Rees T, He Y, McFarlane N (2015) Multiple regimes of wind, stratification, and turbulence in the stable boundary layer. *J Atmos Sci* 72:3178–3198

Monti PF, Chan W, Princevac M, Kowalewski T, Pardyjak E (2002) Observations of flow and turbulence in the nocturnal boundary layer over a slope. *J Atmos Sci* 59:2513–2534

Mortarini L, Stefanello M, Degrazia G, Roberti D, Castelli ST, Anfossi D (2016) Characterization of wind meandering in low-wind-speed conditions. *Boundary-Layer Meteorol* 161:165–182

Mortarini L, Cava D, Giostra U, Acevedo O, Nogueira Martins LG, Soares de Oliveira PE, Anfossi D (2017) Observations of submeso motions and intermittent turbulent mixing across a low level jet with a 132-m tower. *Q J R Meteorol Soc* 144:172–183

Nappo C (1991) Sporadic breakdown of stability in the PBL over simple and complex terrain. *Boundary-Layer Meteorol* 54:69–87

Ohya Y, Nakamura R, Uchida T (2008) Intermittent bursting of turbulence in a stable boundary layer with low-level jet. *Boundary-Layer Meteorol* 126:249–263

Petenko I, Argentini S, Casasanta G, Genton C, Kallistratova M (2019) Stable surface-based turbulent layer during the polar winter at Dome C, Antarctica: Sodar and in situ observations. *Boundary-Layer Meteorol* 171:101–128

Pfister L, Sigmund A, Olesch J, Thomas CK (2017) Nocturnal near-surface temperature but not flow dynamics, can be predicted by microtopography in a mid-range mountain valley. *Boundary-Layer Meteorol* 165:333–348

Pfister L, Sayde Selker J, Mahrt L, Thomas CK (2019) Classifying the nocturnal boundary layer into temperature and flow regimes. *Q J R Meteorol Soc* 145:1515–1534

Poulos G, Blumen W, Fritts D, Lundquist J, Sun J, Burns S, Nappo C, Banta R, Newsome R, Cuxart J, Terradellas E, Balsley B, Jensen M (2001) A comprehensive investigation of the stable nocturnal boundary layer. *Bull Am Meteorol Soc* 83:555–581

Sun J, Burns S, Lenschow D, Banta R, Newsom R, Coulter R, Frasier S, Ince T, Nappo C, Cuxart J, Blumen W, Lee X, Hu XZ (2002) Intermittent turbulence associated with a density current passage in the stable boundary layer. *Boundary-Layer Meteorol* 105:199–219

Sun J, Mahrt L, Banta RM, Pichugina YL (2012) Turbulence regimes and turbulence intermittency in the stable boundary layer during CASES-99. *J Atmos Sci* 69:338–351

Sun J, Mahrt L, Nappo C, Lenschow D (2015a) Wind and temperature oscillations generated by wave-turbulence interactions in the stably stratified boundary layer. *J Atmos Sci* 71:1484–1503

Sun J, Nappo CJ, Mahrt L, Belušić D, Grisogono B, Stauffer DR, Pulido M, Staquet C, Jiang Q, Pouquet A, Yagüe C, Galperin B, Smith RB, Finnigan JJ, Mayor SD, Svensson G, Grachev AA, Neff WD (2015b) Review of wave-turbulence interactions in the stable atmospheric boundary layer. *Rev Geophys.* <https://doi.org/10.1002/2015RG000487>

Tampieri F, Yagüe C, Viana S (2015) The vertical structure of second-order turbulence moments in the stable boundary layer from SABLES98 observations. *Boundary-Layer Meteorol* 157:45–59

Thomas CK, Kennedy A, Selker J, Moretti A, Schroth M, Smoot A, Tufillaro N (2012) High-resolution fibre-optic temperature sensing: a new tool to study the two-dimensional structure of atmospheric surface-layer flow. *Boundary-Layer Meteorol* 142:177–192

Van de Wiel BJH, Ronda R, Moene A, de Bruin H (2002) Intermittent turbulence and oscillations in the stable boundary layer over land. Part I: a bulk model. *J Atmos Sci* 59:942–958

Vercauteren N, Mahrt L, Klein R (2016) Investigation of interactions between scales of motion in the stable boundary layer. *Q J R Meteorol Soc* 142:2424–2433

Vercauteren N, Boyko V, Kaiser A, Belušić D (2019) Statistical investigations of flow structures in different regimes of the stable boundary layer. *Boundary-Layer Meteorol*. <https://doi.org/10.1007/s10546-019-00464-1>

Zeeman MJ, Selker JS, Thomas C (2015) Near-surface motion in the nocturnal, stable boundary layer observed with fibre-optic distributed temperature sensing. *Boundary-Layer Meteorol* 154:189–205

Publisher's Note Springer Nature remains neutral with regard to jurisdictional claims in published maps and institutional affiliations.